COBEM 2021 26th International Congress of Mechanical Engineering
November 22-26, 2021, Virtual Congress, Brazil

COB-2021-1047 DEVELOPMENT OF A PARTICLE TRACKING VELOCIMETRY (PTV) MEASUREMENT TECHNIQUE FOR THE EXPERIMENTAL INVESTIGATION OF OIL DROPS BEHAVIOR IN DISPERSED OIL-WATER TWO-PHASE FLOW WITHIN A CENTRIFUGAL PUMP IMPELLER

Rafael Franklin Lázaro de Cerqueira[2]
Rodolfo Marcilli Perissinotto[1]
William Monte Verde[2]
Jorge Luiz Biazussi[2]
Marcelo Souza de Castro[1]
Antonio Carlos Bannwart[1]
[1]School of Mechanical Engineering, University of Campinas, Mendeleyev Street, 200, Campinas, São Paulo, Brazil
[2]Center for Petroleum Studies, University of Campinas, Cora Coralina Street, 350, Campinas, São Paulo, Brazil

rafaelfc@unicamp.br, rodolfomp@fem.unicamp.br, wmv@unicamp.br, biazussi@unicamp.br, mcastro@fem.unicamp.br, bannwart@fem.unicamp.br

Abstract. *The objective of the current work is to present the development of a robust Particle Tracking Velocimetry (PTV) software for the analysis of the behaviour of oil drops in an oil-water two-phase flow within a centrifugal pump impeller. The tracking was performed through high-speed camera acquisitions in a transparent pump prototype, which enabled the visualization of oil drops dispersed in water in all the impeller channels. The PTV software is based on an U-NET and standard convolutional networks, which detect the oil drop contours in each frame of the high-speed camera videos. In order to assess the PTV software capabilities, a single experiment was analyzed in detail. In this experiment, due to the pump rotation speed and the water flow rate, intense transient fluctuations on the dispersed oil size distribution were observed in the recorded acquisitions. This procedure completely characterized the instantaneous drop dynamics in the pump impeller. According to the results, there is a strong dependence between the oil injection flow rate, the instantaneous drop size distribution, and the average velocity field.*

Keywords: *Particle tracking velocimetry, centrifugal pump, oil drop, two-phase liquid-liquid flow*

1. INTRODUCTION

In oil production, centrifugal pumps are widely used as an artificial lift method. During operation in oil fields, it is usually unavoidable to operate the pump in unfavourable conditions, such as in the presence of gas and viscous fluids in the system. The flow structures and phase arrangements in the impeller cause the pump performance to decay. In this situation, operational instabilities and premature equipment failure may occur as well. Several experimental studies have been performed to better comprehend the phase distribution inside the pump's impeller channels, mainly presenting a qualitative analysis of two-phase flows. The recent work of Perissinotto *et al.* (2021) contains a detailed review of relevant flow visualization studies on centrifugal pumps.

In most of the studies found in the literature, high-speed camera images are used to visualize the flow patterns inside the pump (Zhang *et al.*, 2016; Monte Verde *et al.*, 2017; Zhao *et al.*, 2021). However, only a few of these works attempt to track the dispersed phase's motion and extract quantitative information regarding the dynamics of bubbles or drops (Perissinotto *et al.*, 2019, 2020; Stel *et al.*, 2019).

In Perissinotto *et al.* (2019), the authors tracked the motion of individual oil drops in an oil-water two-phase flow within a centrifugal pump impeller through the use of high-speed camera images. According to the results, there is a clear dependence between the flow conditions and oil drops dynamics. In particular, the authors observed that oil drops flowing close to the impeller's suction blades move faster than those located near the pressure blades. Using the same experimental setup and geometry, the authors in Perissinotto *et al.* (2020) studied the motion of water drops flowing in a water-oil two-phase flow. The analysis of the water drops motion indicated that these drops travel in random trajectories, decelerating as they move towards the impeller exit. In both studies, the flow conditions affected the path of the drops.

In Stel *et al.* (2019), the authors adopted a tracking technique similar to the one used in Perissinotto *et al.* (2019) and Perissinotto *et al.* (2020) to study the bubble dynamics in a gas-liquid two-phase flow in a centrifugal pump impeller.

According to the authors, there is a dependence of the bubble diameters and their trajectories within the impeller channels. The results showed that small bubbles follow a smooth trajectory as they move throughout the channel, from the inlet to the outlet plane, while larger bubbles present a lateral deflected motion.

Despite the rich analysis and discussions presented in Perissinotto *et al.* (2019), Stel *et al.* (2019) and Perissinotto *et al.* (2020), in these studies the dispersed phase motion was tracked through manual operations. This, in turn, may result in insufficient samples which cannot fully describe the dispersed phase dynamics. That is of fundamental importance when those results may provide a better comprehension on the relationship between the dispersed phase and pump performance. In addition, as the formation of emulsions in impellers is a top issue for the oil industry, the quantitative information may help the development of useful phenomenological models, which are crucial to the design and operation of centrifugal pumps employed in oil fields (Bulgarelli *et al.*, 2021).

In recent years, different authors (Poletaev *et al.*, 2020; Haas *et al.*, 2020; Torisaki and Miwa, 2020; Serra *et al.*, 2020; Cerqueira and Paladino, 2021; Cerqueira *et al.*, 2021) proposed deep-learning techniques for identifying, and in some cases, tracking the motion of the dispersed phase in two-phase flows. Recently, in Cerqueira *et al.* (2021), the present author used a U-Net convolutional neural network (Ronneberger *et al.*, 2015), employed for semantic image segmentation tasks, to create a binary mask and remove the gas bubbles in Particle Image Velocimetry (PIV) raw images. Thus, in that previous work, the U-Net generated binary masks which identified the bubbles on the images, creating a mask capable of correctly reconstructing the dispersed phase's shape.

The objective of the current work is to present the development of a robust Particle Tracking Velocimetry (PTV) software for the analysis of oil drops behaviour in dispersed oil-water two-phase flow within a centrifugal pump impeller. High-speed camera images were captured in a transparent pump prototype (Perissinotto *et al.*, 2019, 2020) which enabled the visualization of dispersed oil drops in water in all the impeller channels simultaneously.

In this present work, a U-Net convolutional network identifies and highlights the instantaneous oil drop contours from the flow images. Then, a PTV analysis is carried out with the instantaneous drop positions from those deep-learning processed images. A Convolutional Neural Network (CNN) identification algorithm removes overlapped drop contours. After the oil drops are identified, the processed and classified images are used to compute the instantaneous displacement through a Labelled Object Velocimetry (LOV) technique (Laupsien *et al.*, 2021).

In order to asses the capabilities of the PTV software, a single experiment with an intense transient fluctuation was analyzed in detail with the current technique. The instantaneous Lagrangian results of the PTV algorithm were transformed into an Eulerian coordinate. This transformation allowed the generation of time-averaged fields, which completely characterize the drop dynamics in the impeller channel.

2. EXPERIMENTAL SETUP

Experiments were performed in the apparatus described in Monte Verde *et al.* (2017), Perissinotto *et al.* (2019) and Perissinotto *et al.* (2020). The setup is composed of a water flow line and a black-dyed mineral oil injection system, in addition to a centrifugal pump prototype based on a real pump model commonly used in oil wells. In order to visualize the flow inside the impeller channels, the top shroud was removed and replaced by a new one made of transparent plexiglass. This modification allowed the study of gas-liquid flows in Monte Verde *et al.* (2017) and liquid-liquid flows in Perissinotto *et al.* (2019) and Perissinotto *et al.* (2020). The schematic diagram of the experimental facility is shown in Fig. 1.

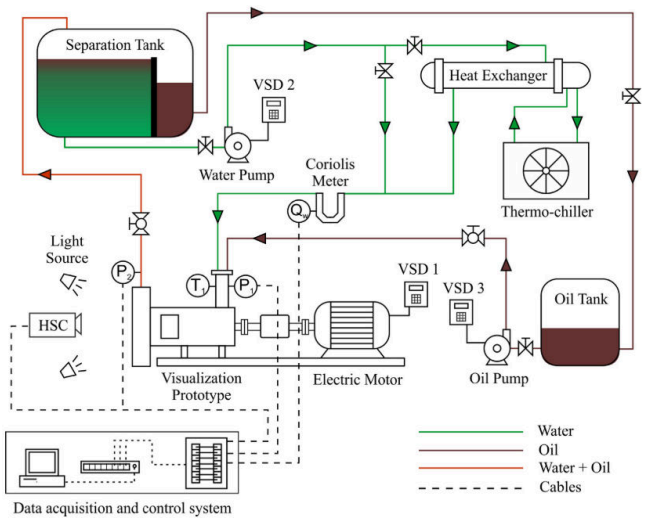

Figure 1: Schematic diagram of the experimental facility. Figure extracted from Perissinotto *et al.* (2019).

3. IMAGE PROCESSING METHOD

In the present work, the U-Net and CNN models and image processing algorithms were developed in the Python programming language. The image processing routines were implemented using the OpenCV (Bradski, 2000) library. For the deep-learning methods, the Keras (Chollet *et al.*, 2015) framework with a Tensorflow (Abadi *et al.*, 2015) backend was employed.

3.1 U-Net model

The U-Net is a convolutional network architecture for precise image segmentation. The neural network can be seen as an encoder-decoder neural network architecture where encoder and decoder layers are directly connected. This layer connection helps the network recover information lost during the max-pooling operations from the encoder module. For more details, the reader may refer to the original U-Net convolutional network architecture implementation (Ronneberger *et al.*, 2015).

In order to train the U-Net convolutional network, the high-speed camera images were manually labelled to create the training datasets. The masks were manually generated by using a simple GUI (Graphical User Interface) software developed for this sole purpose. Through this application, it was possible to approximate the oil drop contours through ellipsoids or, depending on the case, by a contour composed of a set of connected points.

Different U-Net architectures were tested by modifying the hyperparameters of the neural network. After finishing the training step, the U-Net resulting mask was compared against a validation dataset. Therefore, it was possible to quantify the quality of the masks produced by the U-Net model.

Figure 2 presents the U-Net segmentation in two different flow conditions, where the dispersed oil drop morphology differs completely. In Fig. 2a), due to the lower water flow rate ($Q_w = 1.06\ m^3/h$) and pump rotational speed ($N = 300\ rpm$), the oil drops present a large size and a distorted shape. On the opposite, in Fig. 2b), due to the higher water flow rate ($Q_w = 4.26\ m^3/h$) and pump rotational speed ($N = 1200\ rpm$), the oil drops are smaller in size and have an ellipsoidal shape. As observed in these two examples, the trained U-Net is capable of segmenting the images and identifying the drop regions throughout the entire impeller geometry.

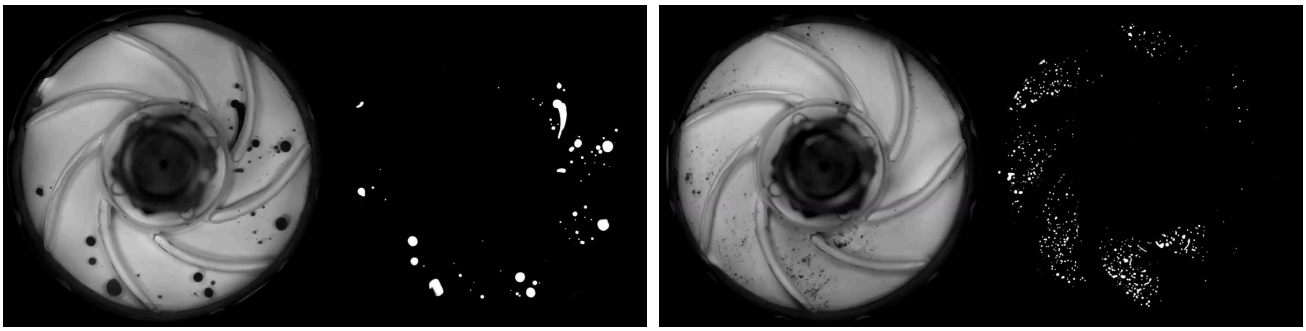

(a) $N = 300\ rpm$ and $Q = 1.06\ m^3/h$ (b) $N = 1200\ rpm$ and $Q = 4.26\ m^3/h$

Figure 2: Example of the image segmentation mask produced by the U-Net model.

3.2 CNN model

Despite successfully reconstructing the dispersed oil drop contours by creating a binary mask, the U-Net model cannot identify if a given contour represents a unique drop or a set of overlapped drops. Therefore, an additional step was added to the image processing pipeline to classify whether a certain contour represents a valid drop. In the present work, this classification task was done by a CNN model. As the U-Net labelling, this model was built from manually labelled images, which were classified with the help of a custom build GUI software.

At the end of the classification step, the contours were classified as "valid" and "invalid", where the ones from the first category had their instantaneous velocity calculated and could be used to produce the ensemble-averaged results, while the "invalid" drops were discarded and not included in the statistical analysis.

As with the U-Net model, different CNN architectures were proposed and compared to a validation dataset. In this case, since the CNN network was simpler than the U-Net architecture, it was possible to use the Keras-Tuner package (Chollet *et al.*, 2015) to run a hyperparameter optimization study. The CNN model classification results, produced by the highest accuracy model from the hyperparameter study, can be visualized in Fig. 3, where a region of the impeller is highlighted and magnified. According to the results, the CNN is capable of identifying drops that are overlapped in different oil drop morphologies.

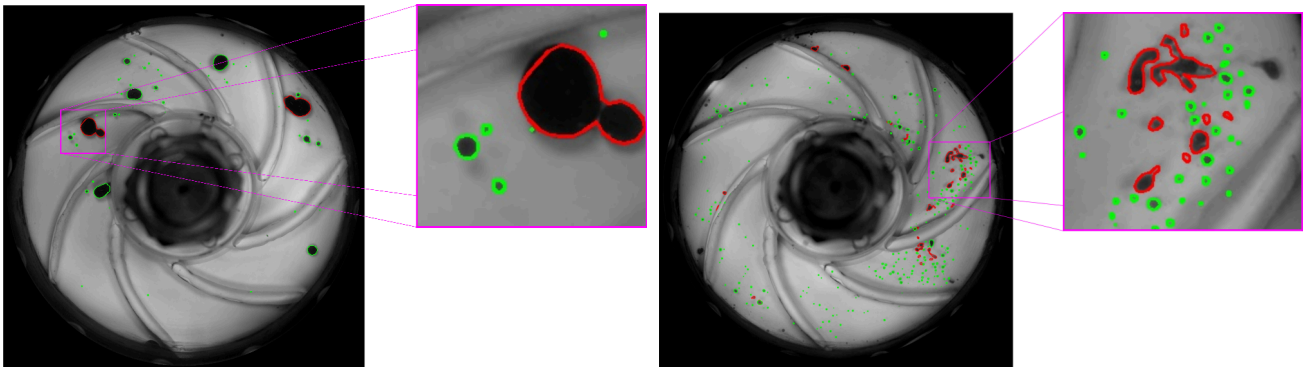

(a) $N = 300\ rpm$ and $Q = 1.06\ m^3/h$ (b) $N = 600\ rpm$ and $Q = 2.13\ m^3/h$

Figure 3: Example of the CNN contour classification in two different flow conditions: a) Flow configuration where the drops present a distorted shape and large characteristic size and b) Flow configuration where the oil drops present a smaller size and an ellipsoidal shape. Contours in red represent "invalid" drops, while the ones in green represent "valid" drops.

4. DROP VELOCITY CALCULATION

After classifying the entire set of contours in a given image, the Labelled Object Velocimetry (LOV) technique (Laupsien *et al.*, 2021) was adopted for obtaining the drop displacement. The LOV is based on spatial correlations similar to those used in Particle Image Velocimetry (PIV), but instead of using images where tracer particles are present, it employs grey-level shadowgraphy images. Here, the calculation is based on the images produced by the U-Net model by using the masked image of two consecutive frames. After determining the displacement of the contour, this value was applied to compute the instantaneous drop velocity by multiplying the pixel displacement by the calibration value (pixel to mm equivalence) and dividing this value by the high-speed camera acquisition frequency.

When applying the PTV technique, most of the available methods found in the literature work by identifying objects over two consecutive images (Cerqueira and Paladino, 2021; Stahnke *et al.*, 2021). By adopting this approach, errors may be incurred in cases involving large deformable objects, such as the dispersed oil drops in the present work. Therefore, the LOV method was preferred over the traditional PTV approach.

As a drawback, since the method relies on a correlation method, i.e., there is not a reciprocal of a given drop in the next image frame, it was necessary to create this link between drops on the i-th and $(i+1)$-th frame. This was done by applying the U-Net and CNN models into the i-th and $(i+1)$-th frames and calculating the LOV displacements. First, the drops found in the i-th frame had their contours projected to the $(i+1)$-th frame. Then, the procedure was executed in the reversed order, where drops from the $(i+1)$-th frames were projected in the i-th frame. When the original and back-propagated contours overlapped, the pairing was completed, and it was possible to reconstruct the drop trajectory. This procedure is schematically represented in Fig. 4, which presents the propagation from the i-th to the $(i+1)$-th frame. In the first frame, the LOV displacements of the identified drops are calculated. In the second frame, only the drops, which also are identified from the CNN and U-Net step, are located. Due to high-speed camera acquisition frequency, some drops may experience a small displacement. Hence, the drop contours from the i-th are superimposed on the $(i+1)$-th frame. If the contours overlap, the contours represent the same drop. In addition, some drops may move a distance larger than their characteristic diameter. In these cases, the drop trajectory is estimated with the LOV velocity in the i-th frame. If the contour in the $(i+1)$-th frame overlaps its trajectory, the contours represent the same drop. To improve the PTV robustness, this same procedure is then repeated in the reverse order, from $(i+1)$-th to i-th frame.

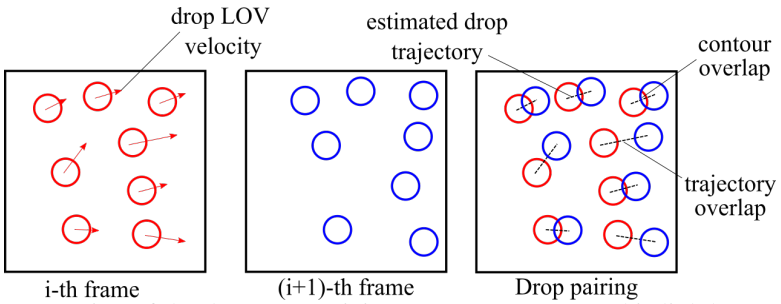

Figure 4: Schematic representation of the drop connectivity, necessary to create this link between drops on the i-th and $(i+1)$-th frame. The dashed lines on the last pane present the estimated drop trajectory by its instantaneous velocity.

The procedures described in this section are performed in each frame of the high-speed camera acquisition. As an

example, Fig. 5a) shows the drops detected on a current frame and their "pairs" found on the next frame, while Fig. 5b) illustrates the instantaneous velocity vectors obtained at a given flow condition.

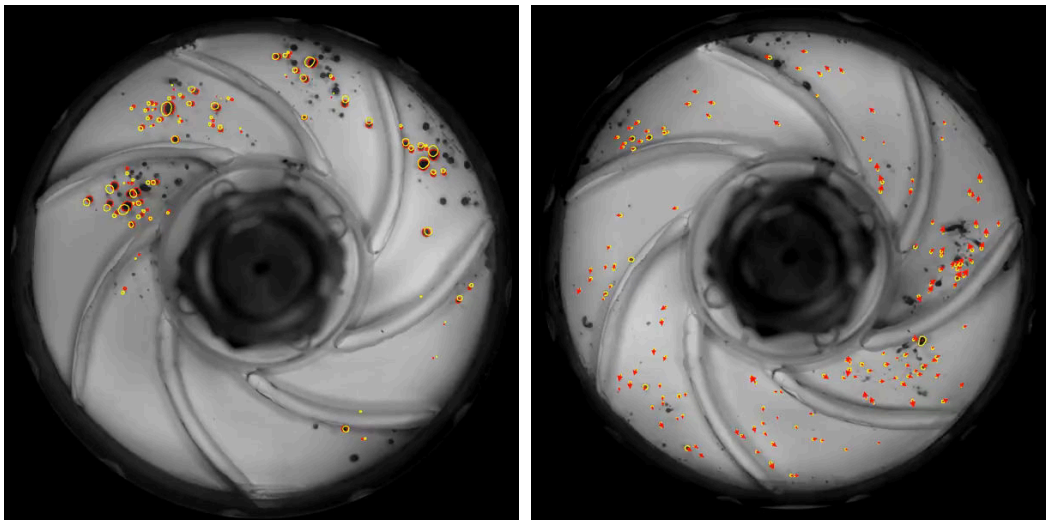

(a) $N = 300\ rpm$ and $Q = 1.06\ m^3/h$ (b) $N = 600\ rpm$ and $Q = 2.13\ m^3/h$

Figure 5: Example of results from the LOV: a) each red contour represents a drop in the current frame, while each yellow contour indicates its shape in the next frame; b) red arrows symbolize the instantaneous velocity vectors of the oil drops flowing in the impeller at a certain flow condition.

5. RESULTS

In Perissinotto *et al.* (2019), when investigating and discussing the data and images from the high-speed camera, the authors took care to only extract experimental results at conditions in which the mineral oil injection was uniform. This was necessary since the dispersed phase was injected through a peristaltic pump which, due to its mechanical design, resulted in a pulsating flow of oil drops in the transparent prototype test section. Therefore, at certain pump operations and flow configurations, a severe fluctuating component was observed in the dispersed oil phase. Thus, some portions of the videos from the high-speed camera had to be discarded when the results were analyzed by the researchers.

On the other hand, in this present work, through the use of an automatic PTV technique, it is now possible to process those results and analyze the effects of the dispersed oil phase flow rate on the oil drop dynamics. Thus, an experimental condition in which those fluctuations were visible was selected to assess the capabilities of the new PTV software and finally analyze the oil drop dynamics. This experimental condition represents the "C1 test" in the study by Perissinotto *et al.* (2019), where the pump rotational speed is $N = 300\ rpm$, the water flow rate entering the impeller sections is $Q_w = 1.06\ m^3/h$ and the oil flow rate is $Q_o = 0.0072\ m^3/h$.

5.1 Instantaneous oil volume fraction

The deep-learning based image processing algorithm developed in the current work was able to detect most of the oil drops present in the images. Therefore, it was possible to estimate the instantaneous oil volume fraction $\varepsilon_o(t)$ from the detected oil drops, calculated as:

$$\varepsilon_o(t) = \frac{\forall_o(t)}{\forall_{impeller}} = \frac{\sum_{i=i}^{n_i} \forall_{o,i}}{\forall_{impeller}} \tag{1}$$

where $\forall_{impeller}$ is the total volume of the impeller channels and $\forall_o(t)$ is the instantaneous total oil volume, which is the sum of the volume $\forall_{o,i}$ of the n_i oil drops detected on a single image frame at a time instant t. In the present work, the oil drops were approximated by prolate spheroids, and their volumes ($\forall_{o,i}$) were estimated as follows:

$$\forall_{o,i} = \frac{1}{6}\pi {d_{i,1}}^2 d_{i,2} \tag{2}$$

where $d_{i,1}$ is the length of the minor axis and $d_{i,2}$ is the length of the major axis of a detected oil drop.

Figure 6 presents the transient oil volume fraction $\varepsilon_o(t)$ for the selected experimental point during the total acquisition time, which was filmed by the high-speed camera at a 1000 fps acquisition rate.

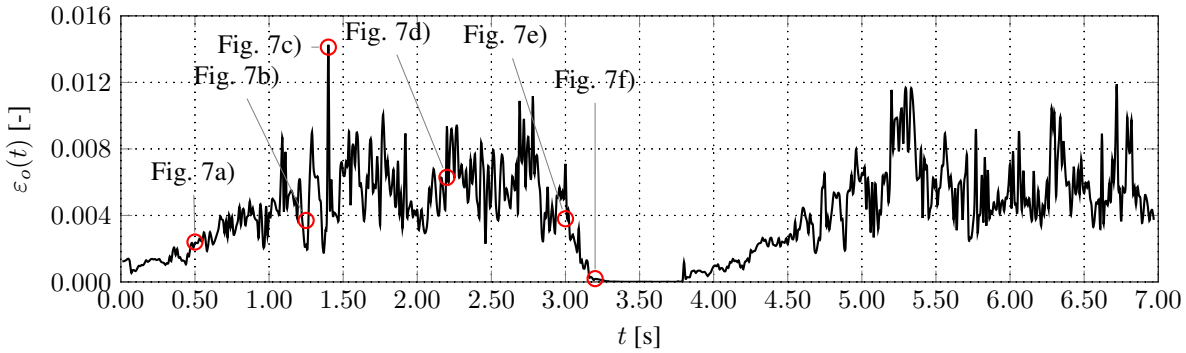

Figure 6: Instantaneous oil volume fraction $\varepsilon_o(t)$ along the acquisition period. The circles and their labels represent the time instant when the images shown in Fig. 7 were taken.

The results of Fig. 6 reveal that indeed the peristaltic pump does not inject the dispersed oil drops uniformly. It is possible to observe that the oil volume fraction first increases, reaches an approximately constant state and then decays to a condition where no oil is present on the test section. According to the transient results, the high-speed camera first acquires a complete oil injection cycle and then captures a part of the second one. In Perissinotto *et al.* (2019), the dynamics of the oil drops were analyzed with video portions related to the uniform region of $V_{o,i}$.

As can be noticed, the transient values of the oil volume fraction in Fig. 6 present strong oscillations from frame to frame. Such deviations are a result of possible occlusions that may occur when multiple oil drops overlap, as stated in Section 3, and also a consequence of the methodology adopted when calculating the oil drop volume.

To better visualize the instantaneous phase distribution within the impeller channels, snapshots of the experimental acquisition are shown in Fig. 7. The time instants when the images were taken are identified in Fig. 6 by a circle and a label. In addition, the two axes from the prolate spheroid approximation are available for each detected drop in Fig. 7.

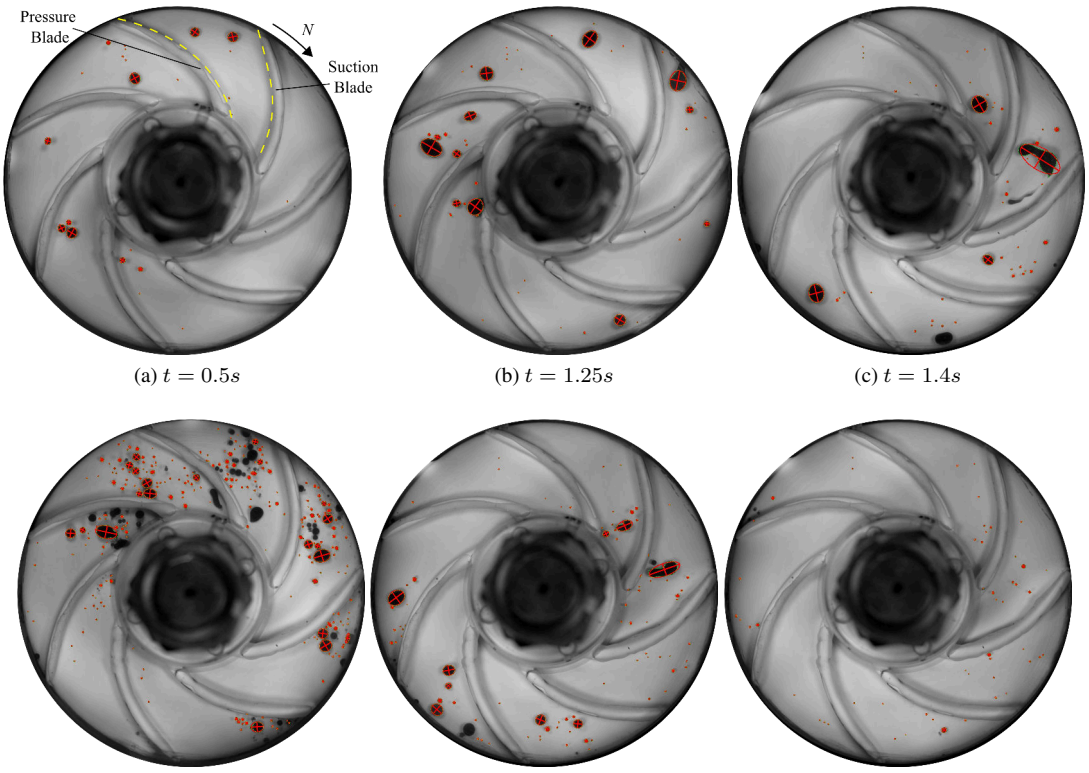

(a) $t = 0.5s$ (b) $t = 1.25s$ (c) $t = 1.4s$

(d) $t = 2.2s$ (e) $t = 3.0s$ (f) $t = 3.2s$

Figure 7: Visualization of the dispersed oil drop distribution in different time instants, illustrating the pulsating characteristic of the oil injection system. In these pictures, the impeller became stationary through the use of an auxiliary image processing algorithm that rotated the image counter-clockwise, following the idea by Perissinotto *et al.* (2019).

The results from Fig. 7 reveal that the drop size distribution changes during the acquisition due to fluctuations in the oil injection system. Following the time coordinate of Fig. 6, as the first injection cycle initiates, the oil drops present a

spheroidal shape, Fig. 7a). As the oil flow rate increases, Figs. 7b) and 7c), the oil drops increase in volume and small drops are also visible in the test section. According to the observations of Perissinotto *et al.* (2019), these small drops are formed outside the impeller channel, and the breakage occurs close to the oil injection point, where the drops undergo a sudden change in direction and momentum. Increasing the oil flow rate further, Fig. 7d), a higher number of smaller drops are visible together with an increased population of larger drops. That is the typical flow configuration found over the "uniform" oil injection regime that lasts from 1.50s until 2.75s in the first oil injection cycle. After this point, the oil flow rate decreases, Fig. 7e), reducing the number of small and large drops until only a few tiny oil drops remain present, Fig. 7f). The same trend is observed in the second oil injection curve, which starts close to $t = 2.75$s and lasts until the end of the high-speed camera acquisition.

In Fig. 7, the highlighted contours represent the detected oil drops returned by the U-Net/CNN model. It is noticeable that, in Fig. 7d), the oil drops that are close to or overlapping their neighbours are not detected. That is the reason why the oil volume fraction value, as shown in Fig. 6, may result in underestimated values. On the contrary, in Fig. 7c), a large deformed drop is approximated by a prolate spheroid, and the oil volume is overestimated. However, despite the associated uncertainty regarding the estimation of the oil volume fraction, the results represent satisfactorily the transient conditions of the oil injection system.

5.2 Time-interval statistics

The automatic PTV developed in the present work is capable of extracting information with regard to the shape and velocity of oil drops at any instant of time. However, instantaneous results may not provide sufficient information about the drop dynamics, in special when the results are analyzed in Eulerian coordinates, which is the present case. Therefore, in order to better comprehend the effect of the instantaneous oil volume fraction and size distribution on the drop dynamics, a time-interval statistical procedure was adopted.

Through this procedure, instead of producing statistical results over the entire high-speed camera acquisition, i.e., from t = 0.0s to t = 7.0s, a short sampling interval was defined to average the instantaneous fields. Hence, it was possible to study the transient drop size distribution and the average drop velocity field as oil was injected into the impeller channels. Following the rotational nature of the impeller motion, the sampling time was based on the time necessary for the impeller to complete a full revolution (0.2s). According to preliminary analysis, a time interval of 0.6s, time to complete three full revolutions, resulted in consistent averaged results.

5.2.1 Drop size distribution

Figure 8 displays the drop size distribution at three different instants of the oil injection cycle. In these results, the Sauter mean diameter d_{32}, which is the ratio of volume to surface area (Crowe *et al.*, 2011), is adopted to characterize the size of the oil drops.

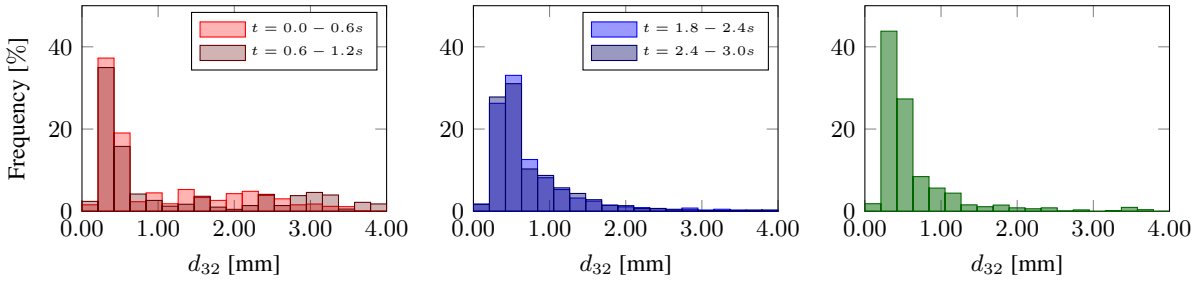

(a) $t = 0.0s - 1.2s$, $\overline{\langle d_{32} \rangle}$ = 1.28mm (b) $t = 1.8s - 3.0s$, $\overline{\langle d_{32} \rangle}$ = 0.82mm (c) $t = 3.0s - 3.6s$, $\overline{\langle d_{32} \rangle}$ = 0.78mm

Figure 8: Drop size distribution in three different moments of the oil injection cycle. These histograms refer to the results of the first injection cycle, $t = 0.0 - 3.6s$, as show in Fig. 6. The $\overline{\langle d_{32} \rangle}$ variable denotes the mean drop diameter in each frequency plot.

The drop size distributions from Fig. 8a) reveal that, in the first moments, when the oil volume fraction is low, most drops have a small diameter in the range between 0.0 and 0.75mm. As observed, Fig. 8a) present the drop size distribution in two intervals of the initial injection cycle. There is a large difference in these two distributions, which indicates a transient component in the drop injection cycle. Besides, in both time intervals, drops larger than 0.75mm assume an uniform distribution, suggesting that when the peristaltic pump injects oil into the test section, the large drops do not have a preferential shape. As the oil volume fraction increases and the injection cycle reaches an uniform state, Fig. 8b), the mean drop diameter shifts to a smaller value, and large drops ($d_{32} > 2.5$ mm) are rarely found throughout the impeller channels. Another important observation of Fig. 8b) is that, within the time interval when the oil volume fraction

is constant, the drop size distribution remains the same, with minor differences. However, at the end of the injection cycle, Fig. 8c), the mean drop diameter moves toward smaller values, and a few occasional large drops are present in the prototype test section. The distributions shown in Fig. 8 are relative to the first oil injection cycle (see Fig. 6), but the observations were reported in the second cycle as well.

5.2.2 Drop velocity

The results presented so far indicate that not only the instantaneous oil volume fraction exhibits a transient/cycling behaviour, but also its size distribution does. Hence, this section is devoted to present time-interval results of the velocity field, aiming to verify whether the differences identified in the oil volume fraction and size distribution also influence the dispersed phase's dynamics.

This section provides the velocity as a time-interval averaged field in a "representative" impeller channel. This procedure was adopted by taking advantage of the symmetry between the impeller channels and the pump prototype design. Since the blade geometry is the same within the whole impeller and the inlet region distributes the flow equally to the channels, it was possible to consider that the flow characteristics and structures are the same in each channel. This approach increased the number of samples and the consistency of the results in each time-interval averaged field. Therefore, a mapping function was used to map the values of the different impeller channels to this single representative channel.

In order to compute the time-interval average velocities, the instantaneous drop velocities evaluated by the LOV technique were mapped back to a fixed Eulerian background mesh (Cerqueira and Paladino, 2021). Then, those values were stored in a multidimensional array and an the time-averaged fields were calculated as:

$$\langle \Phi(x,y) \rangle = \frac{\sum_{i=0}^{n_{hold}} \Phi_i(x,y)}{n_{hold}} \tag{3}$$

where n_{hold} is the number of drops acquired in a (x,y) mesh position. The Φ property is a generic variable, such as the drop velocity $\vec{v}_o$. It is important to mention that this calculation was performed in a non-inertial frame of reference (Perissinotto *et al.*, 2019), where the impeller was kept stationary through the help of an auxiliary image processing algorithm.

Figure 9 displays the contour plots of the time-interval averaged velocity magnitude $|\langle \vec{v}_o \rangle|$ of the oil drops in different intervals of the oil injection. The results show that indeed the oil volume fraction and size distribution modify the drop dynamics.

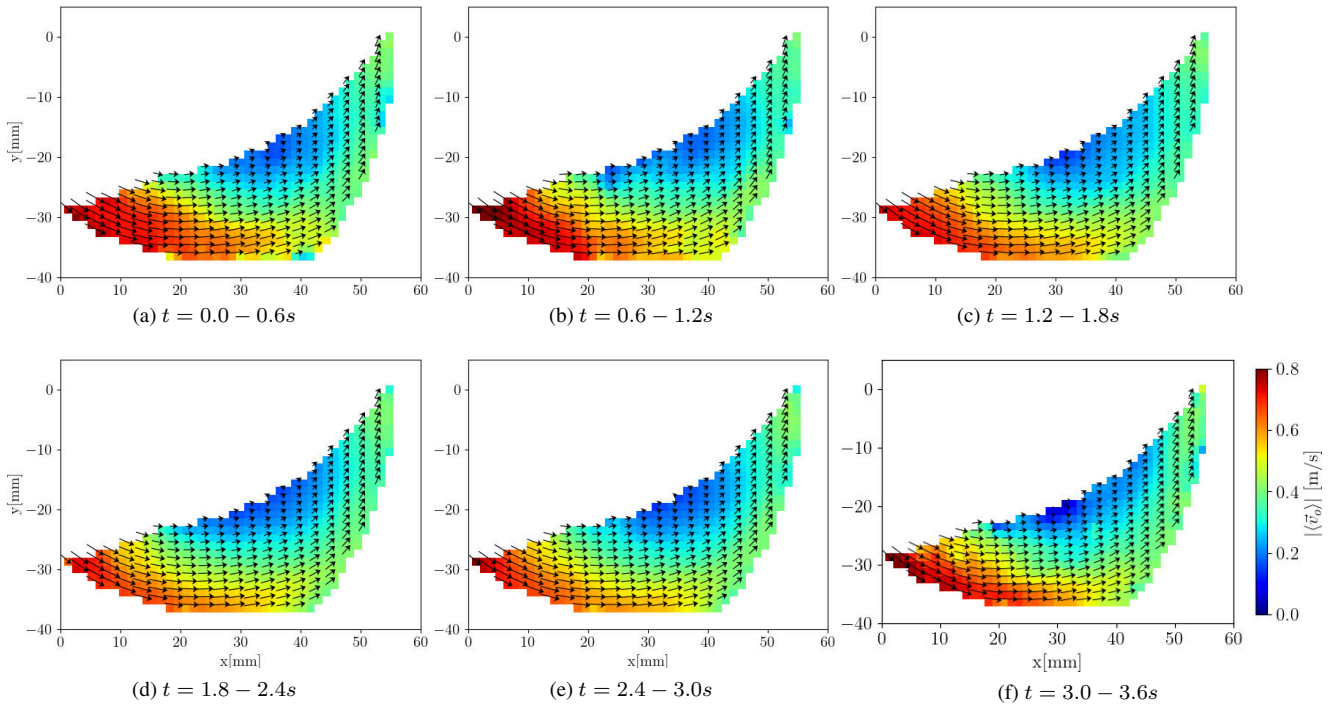

(a) $t = 0.0 - 0.6s$ (b) $t = 0.6 - 1.2s$ (c) $t = 1.2 - 1.8s$

(d) $t = 1.8 - 2.4s$ (e) $t = 2.4 - 3.0s$ (f) $t = 3.0 - 3.6s$

Figure 9: Time-interval averaged velocity magnitude $|\langle \vec{v}_o \rangle|$ of the oil drops in different intervals of the oil injection. The impeller moves clockwise. The pressure blade is at the top and the suction blade is at the bottom of the channel (see Fig. 7).

As expected, the velocity contours shown in Figs. 9d) and e) do not present significant deviations, as those two results represent time-averaged results in two periods when the peristaltic pump was injecting the oil almost uniformly. That

is not the case outside this constant state, as can be observed in Figs 9a)-c) and f). According to these results, large deviations are found in two localized regions. The first one spans from the inlet section to the suction blade, while the second one is near the pressure blade. When comparing those values, it is assumed that the water velocity fields are not altered by the pulsating injection of the peristaltic pump. That is a reasonable assumption, since the volumetric flow rate ratio $\beta_o = Q_o/(Q_w + Q_o)$ and oil volume fractions ε_o present very low values. Therefore, the observed differences may be a consequence of the drop size distribution.

The motion of the oil drops is determined by Newton's second law, and the force acting on each drop may be divided into different hydrodynamic contributions, such as drag, lift, virtual mass and pressure gradient (Crowe *et al.*, 2011). According to the drop size distribution shown in Fig. 8, the main difference between the cases that lie on the uniform oil injection interval and the remainders is the increase in the number of larger or smaller drops. At a steady continuous phase velocity field, the small drops require a lower force to be dragged through the channel. In other words, the velocity of a drop tends to increase as it becomes smaller. In the opposite way, the large drops may demand a higher contribution of the drag force to move, so their velocities may occasionally decrease. Nevertheless, those drops, due to their larger size, may present higher local velocities as a consequence of the pressure gradients acting on them. This partially explains why the time-averaged velocity fields in Figs. 9a) and b) have higher magnitudes at the entrance region, where the pressure gradient is probably more significant. In addition, there is an additional contribution of the impeller rotation: a large drop has a large mass, so it experiences a more intense effect of the centrifugal force, which leads the drop to accelerate.

In summary, the motion of the drops is governed by different force contributions, and the effect of the size distribution on the drop dynamics must be further studied with sophisticated experimental techniques, such as by the use of the PIV technique or by detailed numerical simulations.

6. CONCLUSIONS

In the present study, a Particle Tracking Velocimetry (PTV) software was developed to track the motion of oil drops in a oil-water two-phase dispersion within a centrifugal pump impeller. The motion tracking was done through the image processing of high-speed camera videos of the flow in a transparent pump prototype.

The image processing was based on two deep-learning techniques. First, a U-Net network segmented the high-speed camera images, dividing regions into two categories, one for background and a second one highlighting the oil drop contours. Later, a standard CNN classified each detected oil drop contour as valid or invalid. After detecting the oil drops in each high-speed camera frame, the LOV technique calculated the instantaneous drop velocity.

In order to assess the PTV software capabilities, a single experiment, where the oil drops were injected into the impeller channels in a transient fashion, was analyzed in detail. According to the results, there is a deep dependence between the oil injection flow rate, the instantaneous drop size distribution, and the average velocity field.

The automatic PTV technique detailed in the current work is an advance of the manual procedure described in Perissinotto *et al.* (2019) and Perissinotto *et al.* (2020). The new approach is able to extract much more information from high-speed camera images, making it suitable for analyzing dispersion and emulsion flows within rotating environments. Therefore, the new automatic PTV technique can be further used to increase the comprehension of scientists and researchers on the drop dynamics in the whole impeller, including the study of transient phenomena which may influence the performance of centrifugal pumps used in the oil and gas industry.

7. ACKNOWLEDGEMENTS

We gratefully acknowledge the support of EPIC – Energy Production Innovation Center, hosted by the University of Campinas (UNICAMP) and sponsored by Equinor Brazil and FAPESP – São Paulo Research Foundation (2017/15736-3 and 2020/15140-6). We acknowledge the support of ANP (Brazil's National Oil, Natural Gas and Biofuels Agency) through the R&D levy regulation. Acknowledgements are extended to the Center for Petroleum Studies (CEPETRO) and the School of Mechanical Engineering (FEM) and ALFA Research Group. Prof. Marcelo Castro acknowledges CNPq (National Council for Scientific and Technological Development, Brazil) for the grant given under Contract Number 310191/2020-3.

8. REFERENCES

Abadi, M. *et al.*, 2015. "TensorFlow: Large-scale machine learning on heterogeneous systems". URL `http://tensorflow.org/`. Software available from tensorflow.org.

Bradski, G., 2000. "The OpenCV Library". *Dr. Dobb's Journal of Software Tools*.

Bulgarelli, N.A.V., Biazussi, J.L., Monte Verde, W., Perles, C.E., de Castro, M.S. and Bannwart, A.C., 2021. "Experimental investigation on the performance of Electrical Submersible Pump (ESP) operating with unstable water/oil emulsions". *Journal of Petroleum Science and Engineering*, Vol. 197, No. September 2020, p. 107900. ISSN 09204105. doi:10.1016/j.petrol.2020.107900. URL `https://doi.org/10.1016/j.petrol.2020.107900`.

Cerqueira, R.F., Cerutti, M.A. and Paladino, E.E., 2021. "A deep-learning-based image processing technique for the measurement of two-phase bubbly flows using particle image velocimetry (PIV)". *Proceedings of the 6th Multiphase Flow Journeys, 2021, Online*.

Cerqueira, R.F. and Paladino, E.E., 2021. "Development of a deep learning-based image processing technique for bubble pattern recognition and shape reconstruction in dense bubbly flows". *Chemical Engineering Science*, Vol. 230, p. 116163.

Chollet, F. *et al.*, 2015. "Keras". `https://keras.io`.

Crowe, C.T., Schwarzkopf, J.D., Sommerfeld, M. and Tsuji, Y., 2011. *Multiphase Flows with Droplets and Particles*. CRC Press.

Haas, T., Schubert, C., Eickhoff, M. and Pfeifer, H., 2020. "BubCNN : Bubble detection using Faster RCNN and shape regression network". *Chemical Engineering Science*, Vol. 216, p. 115467. ISSN 0009-2509. doi: 10.1016/j.ces.2019.115467.

Laupsien, D., Men, C.L., Cockx, A. and Line, A., 2021. "Labelled Object Velocimetry: Simultaneous Measurements of Bubble Size and Velocity". *Chemical Engineering Science*, Vol. 230, p. 116180. ISSN 00092509. doi: 10.1016/j.ces.2020.116180. URL `https://doi.org/10.1016/j.ces.2020.116180`.

Monte Verde, W., Biazussi, J.L., Sassim, N.A. and Bannwart, A.C., 2017. "Experimental study of gas-liquid two-phase flow patterns within centrifugal pumps impellers". *Experimental Thermal and Fluid Science*, Vol. 85, pp. 37–51. ISSN 08941777. doi:10.1016/j.expthermflusci.2017.02.019. URL `http://dx.doi.org/10.1016/j.expthermflusci.2017.02.019`.

Perissinotto, R.M., Monte Verde, W., Biazussi, J.L., Bulgarelli, N.A.V., Fonseca, W.D.P., de Castro, M.S., Franklin, E.d.M. and Bannwart, A.C., 2021. "Flow visualization in centrifugal pumps: A review of methods and experimental studies". *Journal of Petroleum Science and Engineering*, Vol. 203, No. January, p. 108582. ISSN 09204105. doi: 10.1016/j.petrol.2021.108582. URL `https://doi.org/10.1016/j.petrol.2021.108582`.

Perissinotto, R.M., Monte Verde, W., de Castro, M.S., Biazussi, J.L., Estevam, V. and Bannwart, A.C., 2019. "Experimental investigation of oil drops behavior in dispersed oil-water two-phase flow within a centrifugal pump impeller". *Experimental Thermal and Fluid Science*, Vol. 105, No. November 2018, pp. 11–26. ISSN 08941777. doi: 10.1016/j.expthermflusci.2019.03.009. URL `https://doi.org/10.1016/j.expthermflusci.2019.03.009`.

Perissinotto, R.M., Monte Verde, W., Perles, C.E., Biazussi, J.L., de Castro, M.S. and Bannwart, A.C., 2020. "Experimental analysis on the behavior of water drops dispersed in oil within a centrifugal pump impeller". *Experimental Thermal and Fluid Science*, Vol. 112, No. November 2019, p. 109969. ISSN 08941777. doi: 10.1016/j.expthermflusci.2019.109969. URL `https://doi.org/10.1016/j.expthermflusci.2019.109969`.

Poletaev, I., Tokarev, M.P. and Pervunin, K.S., 2020. "Bubble Recognition Using Neural Networks: Application to the Analysis of a Two-Phase Bubbly Jet". *International Journal of Multiphase Flow*, p. 103194. ISSN 0301-9322. doi:10.1016/j.ijmultiphaseflow.2019.103194. URL `https://doi.org/10.1016/j.ijmultiphaseflow.2019.103194`.

Ronneberger, O., Fischer, P. and Brox, T., 2015. "U-net: Convolutional networks for biomedical image segmentation". In *International Conference on Medical image computing and computer-assisted intervention*. Springer, pp. 234–241.

Serra, P.L., Masotti, P.H., Rocha, M.S., de Andrade, D.A., Torres, W.M. and de Mesquita, R.N., 2020. "Two-phase flow void fraction estimation based on bubble image segmentation using randomized hough transform with neural network (rhtn)". *Progress in Nuclear Energy*, Vol. 118, p. 103133.

Stahnke, C., Karp, J.R., Santos, P.H., da Silva, F.S. and Morales, R.E., 2021. "Kinematics of droplets and bubbles flowing in a liquid stream". *Journal of Petroleum Science and Engineering*, Vol. 202, p. 108550.

Stel, H., Ofuchi, E.M., Sabino, R.H., Ancajima, F.C., Bertoldi, D., Marcelino Neto, M.A. and Morales, R.E., 2019. "Investigation of the motion of bubbles in a centrifugal pump impeller". *Journal of Fluids Engineering, Transactions of the ASME*, Vol. 141, No. 3, pp. 1–14. ISSN 1528901X. doi:10.1115/1.4041230.

Torisaki, S. and Miwa, S., 2020. "Robust bubble feature extraction in gas-liquid two-phase flow using object detection technique". *Journal of Nuclear Science and Technology*, Vol. 57, No. 11, pp. 1231–1244.

Zhang, J., Cai, S., Li, Y., Zhu, H. and Zhang, Y., 2016. "Visualization study of gas-liquid two-phase flow patterns inside a three-stage rotodynamic multiphase pump". *Experimental Thermal and Fluid Science*, Vol. 70, pp. 125–138. ISSN 08941777. doi:10.1016/j.expthermflusci.2015.08.013. URL `http://dx.doi.org/10.1016/j.expthermflusci.2015.08.013`.

Zhao, L., Chang, Z., Zhang, Z., Huang, R. and He, D., 2021. "Visualization of gas-liquid flow pattern in a centrifugal pump impeller and its influence on the pump performance". *Measurement: Sensors*, Vol. 13, No. November 2020, p. 100033. ISSN 26659174. doi:10.1016/j.measen.2020.100033. URL `https://doi.org/10.1016/j.measen.2020.100033`.

9. RESPONSIBILITY NOTICE

The authors are solely responsible for the printed material included in this paper.